Meteotsunami generation by tropical cyclone rainbands: nearshore effects of rainband dynamics and storm surge

Katherine Anarde[1], Wei Cheng[2], Marion Tissier[3], Jens Figlus[4], and Juan Horrillo[2]

[1]University of North Carolina - Chapel Hill
[2]Texas A&M University at Galveston
[3]Faculty of Civil Engineering and Geosciences, Delft University of Technology
[4]Texas A&M University

November 21, 2022

Abstract

During tropical cyclones, meteotsunami waves can be triggered by atmospheric disturbances accompanying tropical cyclone rainbands (TCRs). Due to a paucity of high resolution field data along open coasts during these extreme events, relatively little is known about meteotsunami generation by TCRs and the coastal impact of these wave phenomena. Here we link high-resolution field measurements of sea-level and air pressure from Hurricane Harvey (2017) with a numerical model to show that large drops in air pressure accompanying trains of very narrow TCRs can initiate meteotsunami O(40 cm) in height along open coasts distant from the storm center (>200 km). The resonant-amplification and propagation of meteotsunami generated by pressure forcing is highly dependent on oceanographic (storm surge, bathymetry, and coastal morphology) and atmospheric factors (variable TCR forward speed, TCR path of translation). We discover that meteotsunami hazard can extend several days before and after hurricane landfall, and that meteotsunami are more ubiquitous along the open coast than tidal gauge records suggest, likely due to the highly-localized propagation and inherent structure of TCRs. This combined field and numerical study identifies the potential, but sometimes highly localized conditions necessary, for meteotsunami to modify storm processes (e.g., overwash, beach erosion) and serve as a coastal flood hazard during hurricane impact.

Meteotsunami generation by tropical cyclone rainbands: nearshore effects of rainband dynamics and storm surge

Katherine Anarde[1*], Wei Cheng[2], Marion Tissier[3], Jens Figlus[2], Juan Horrillo[2]

[1]Department of Civil and Environmental Engineering, Rice University, Houston, Texas, USA
[2]Department of Ocean Engineering, Texas A&M University, Galveston, Texas, USA
[3]Faculty of Civil Engineering and Geosciences, Delft University of Technology, Delft, Netherlands

Key Points:

- Meteotsunami are more ubiquitous in the nearshore during tropical cyclones (TCs) than tidal gauges suggest
- Air pressure anomalies accompanying outer TC rainbands can trigger meteotsunami $O(0.4\text{ m})$ in height and with periods $O(20\text{ min})$
- Meteotsunami can be highly localized and dependent on atmospheric and oceanographic factors, including storm surge

*Current address, Department of Geological Sciences, University of North Carolina at Chapel Hill, Chapel Hill, North Carolina, USA

Corresponding author: Katherine Anarde, `kanarde@unc.edu`

Abstract

During tropical cyclones, meteotsunami waves can be triggered by atmospheric disturbances accompanying tropical cyclone rainbands (TCRs). Due to a paucity of high resolution field data along open coasts during these extreme events, relatively little is known about meteotsunami generation by TCRs and the coastal impact of these wave phenomena. Here we link high-resolution field measurements of sea-level and air pressure from Hurricane Harvey (2017) with a numerical model to show that large drops in air pressure accompanying trains of very narrow TCRs can initiate meteotsunami $O(40$ cm) in height along open coasts distant from the storm center (>200 km). The resonant-amplification and propagation of meteotsunami generated by pressure forcing is highly dependent on oceanographic (storm surge, bathymetry, and coastal morphology) and atmospheric factors (variable TCR forward speed, TCR path of translation). We discover that meteotsunami hazard can extend several days before and after hurricane landfall, and that meteotsunami are more ubiquitous along the open coast than tidal gauge records suggest, likely due to the highly-localized propagation and inherent structure of TCRs. This combined field and numerical study identifies the potential, but sometimes highly localized conditions necessary, for meteotsunami to modify storm processes (e.g., overwash, beach erosion) and serve as a coastal flood hazard during hurricane impact.

Plain Language Summary

During tropical cyclones, spiral rainbands distant from the storm center can trigger small variations in sea level known as meteorological tsunami ("meteotsunami"). Relatively little is known about the forcing that initiates these waves and the beach hazards they pose as it is challenging to collect field data during storm impact. This paper combines new field measurements collected during Hurricane Harvey (2017) with model simulations to show that large drops in air pressure accompanying passage of narrow spiral rainbands can initiate meteotsunami approximately 40 cm in height along open coasts more than 200 km away from storm landfall. Simulations show that the size of these waves depends on oceanographic and storm-specific factors, including the amount of storm surge. We discover that meteotsunami occur frequently along open coasts during tropical cyclones. The beach hazard associated with this phenomenon can be highly localized and extend several days before and after hurricane landfall.

1 Introduction

Observational evidence has shown that tropical cyclones (TCs) can initiate tsunami-like variations in sea level with periods of several minutes to hours (Mercer et al., 2002; Mecking et al., 2009; Olabarrieta et al., 2017; Dusek et al., 2019; Shi et al., 2020). Tidal gauge records suggest that meteorological tsunami ("meteotsunami") are common in the Gulf of Mexico (GOM) and along Florida's Atlantic Coast during TCs, triggered by atmospheric disturbances accompanying tropical cyclone rainbands (TCRs) (Shi et al., 2020). Meteotsunami contributions to total water levels at tidal gauge locations during TCs can be significant (e.g., maximum crest elevation of 0.78 in a mean water depth of $\sim$6 m, Shi et al. (2020)), and may also represent a hazard along beaches through initiation of extreme wave runup (e.g., the Daytona Beach 1992 meteotsunami, Churchill et al. (1995)), rip currents (Linares et al., 2019), and dune and beach erosion. However, given the sheltered locations of tidal gauges along U.S. coasts (i.e., within estuaries, harbors, and bays), and scarcity of field data close to shore during extreme events, relatively little is known about meteotsunami hazard along open coasts during TCs.

Meteotsunami generation on open coasts is typically a multi-resonant process (Monserrat et al., 2006). First, sudden changes in air pressure and/or wind speed associated with a moving-atmospheric disturbance (e.g., storm, squall, frontal passage, or atmospheric gravity wave) produce a small water level perturbation on the continental shelf due to the inverse barometer effect. This perturbation can become strongly amplified as it propagates with the disturbance, first due to external resonance processes and later as a free wave due to nearshore wave transformations such as shoaling, refraction, and superposition of incident and reflected waves. Maximum energy transfer from the atmosphere to the ocean occurs when the speed of the disturbance approaches the shallow water wave celerity (Froude number near 1), a phenomenon called Proudman resonance (Proudman, 1929). Upon reaching the coast, additional resonance effects, such as the matching of harbor seiche periods, are required for the free wave to reach destructive heights (up to several meters) - a phenomenon that has been observed in coastal basins around the world (Rabinovich, 2019).

Using a coupled ocean and atmospheric modeling framework, Shi et al. (2020) showed that for an idealized TC (and simplified bathymetry), wind stress dominates over pressure forcing for meteotsunami generation by TCRs. The numerically simulated meteotsunami were similar to those observed in tidal gauge records, both in frequency (1-2 hr periods), maximum crest elevation ($\sim$0.2-0.4 m), and sequence (either single peak or sequential meteotsunami). Single peak meteotsunami were found to be driven by "outer" TCRs – that is, rainbands that are distant from the inner core of the hurricane – and sequential meteotsunami by trains of principal and secondary rainbands ("inner" TCRs) within the inner core region. Notably, when using only pressure forcing to simulate TCR propagation, the modeled sea-level anomalies generally followed the inverse barometer effect and were not amplified through resonance processes.

During Hurricane Harvey (2017), in-situ measurements of sea level from nearshore environments along the Texas coast showed variability in the meteotsunami frequency band during passage of outer TCRs (here, $\sim$200 km from the storm center), albeit with periods shorter than that modeled by Shi et al. (2020) (here, $\sim$8 to 45 min periods). For the time period proximate to hurricane landfall, trains of outer TCRs with very small horizontal scales ($<$50 km in arc-length) passed frequently over one field site (typically every $\sim$30 minutes) and co-located observations of air pressure showed that they were accompanied by large drops in air pressure. Here we test the hypothesis that many of these very-low frequency sea-level anomalies are meteotsunami initiated by atmospheric disturbances accompanying TCRs. In the absence of co-located measurements of wind forcing, we numerically model the generation potential of meteotsunami by a very-narrow outer TCR using pressure forcing alone. By linking high resolution field measurements with numerical simulation, we show that large drops in air pressure $O(2\text{ mbar})$ associated with trains of outer TCRs can trigger meteotsunami similar to observations of sea-level anomalies in the nearshore, both in period $O(20\text{ min})$ and height $O(0.4\text{ m})$, via Proudman resonant wave growth.

2 Observations

Continuous measurements of sea level from two nearshore environments along the Texas coast showed variability at frequencies f below infragravity waves ($f < 3$ mHz, $>$5.6 min periods), but above known tidal constituents and storm surge ($f > 0.1$ mHz, $<$2.8 hr periods) episodically during Hurricane Harvey (2017). For a complete description of both field sites, instrumentation, as well as a synopsis of Hurricane Harvey's impact, the reader is directed to Anarde et al., (*in review*) and Blake & Zelinsky (2018). Herein, we examine observations of very-low frequency ("VLF", 5.6 min to 2.8 hr periods) wave phenomena over a period of $\sim$4 days in the surf zone and back barrier at Follets Island (Figure 1a), a barrier island located $\sim$200 km northeast of hurricane landfall along the upper Texas Gulf coast. Sea-level fluctuations with periods upwards of 10 min have been observed in surf zones on beaches elsewhere, with generation mechanisms typically attributed to shear instability of the alongshore current (Oltman-Shay et al., 1989) or forcing from wave groups (Haller et al., 1999) (i.e., shear waves). The VLF sea-level anomalies observed in the surf zone during Hurricane Harvey were relatively large (maximum peak-to-trough wave height = 42 cm, Figure 1d) and much lower in frequency and span a larger frequency range (~8 to 45 min periods) than is typical of shear waves, suggesting an alternative or additional generation mechanism(s).

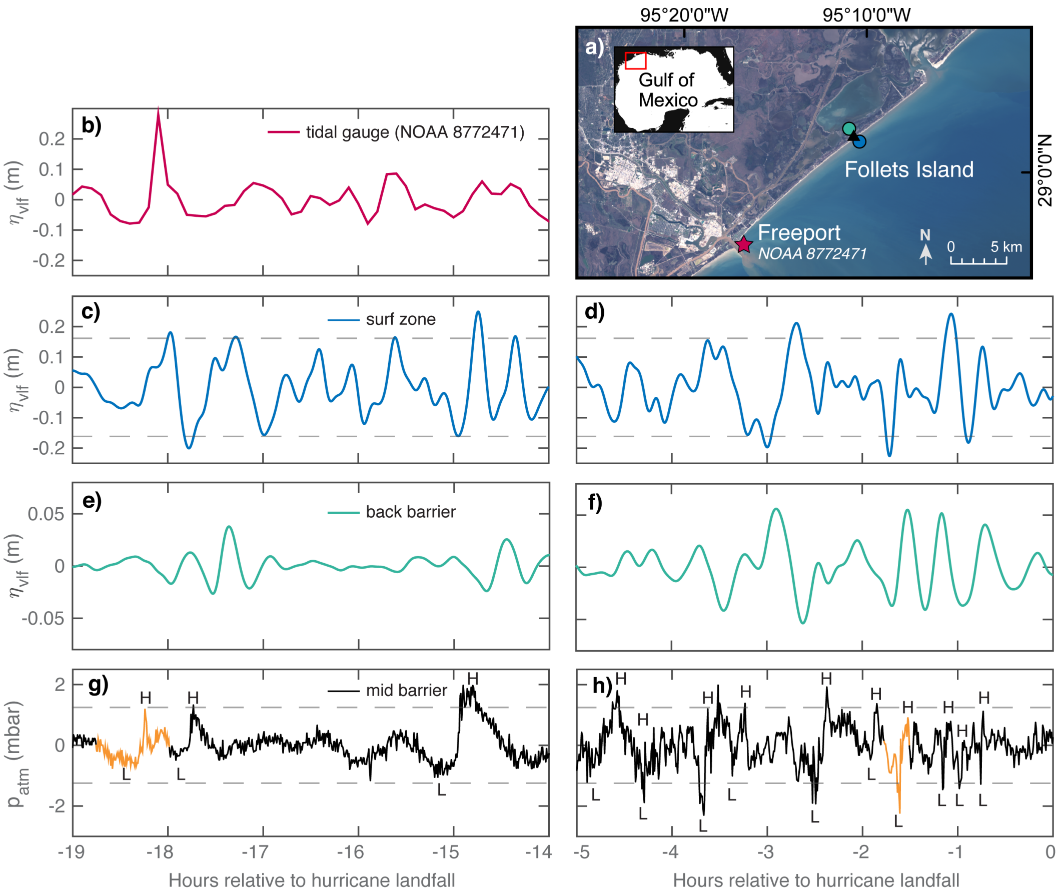

Figure 1. a) Field site location; b-f) the VLF sea-level anomaly η_{vlf} measured at NOAA tidal gauge 8772471 (located within the Freeport harbor 14 km southwest of the site, NOAA (2017)) and in the surf zone and back-barrier environments at Follets Island for two time intervals of elevated η_{vlf}; and high-frequency air pressure p_{atm} ($f > 0.1$ mHz) recorded at Follets Island. The dashed lines in (c-d) and (g-h) denote 3-standard deviations (σ) for η_{vlf} and p_{atm} (respectively). Air pressure disturbances are identified in (g-h) as pressure couplets with a peak ("H") or trough ("L") amplitude that exceeds 3σ (± 1.25 mbar). The disturbances highlighted orange correspond to the land-falling TCRs (bands of high reflectivity) at Follets Island in Figure 3a and b (respectively).

As shown in Figure 2c, relatively large sea-level anomalies (η) were observed at VLF (subscript vlf) during three time intervals over the study period at the Follets Island field site: -18.5 to -14 hrs, -3 to 3 hrs, and 23.5 to 34 hrs relative to hurricane landfall. These time periods were identified by sequential instances of η_{vlf} in the surf zone that exceeded (in absolute value) a threshold of 3 times the standard deviation (σ) of η_{vlf} (dashed lines, Figure 2c), where time series were bandpass filtered with a low-frequency cutoff of 0.1 mHz (2.8 hrs) and high-frequency cutoff of 3 mHz (5.6 min) to isolate η_{vlf}. While arbitrary, this threshold (0.16 m) allows for a more targeted examination of forcing mechanisms responsible for generation of the largest VLF oscillations. Relatively large instances of η_{vlf} were also observed in the back barrier during each of these time periods, albeit these sea-level anomalies were small in magnitude (<5 cm). Notably, the back barrier environment was only hydraulically connected to the nearshore through a tidal inlet located 8 km northeast of the field site (San Luis Pass) and via the Freeport harbor located 15 km southwest of the site (Figure 1a) for the duration of the storm (i.e., no storm overwash or island breaching occurred in the vicinity of the site). Tidal gauges operated by the National Oceanic and Atmospheric Administration (NOAA) within Freeport harbor (Figure 2d) and at San Luis Pass (not shown) also showed water level variability at VLF, however, only the Freeport harbor gauge measured a VLF anomaly of similar magnitude to the surf zone oscillations (0.35 m in height at -18 hrs).

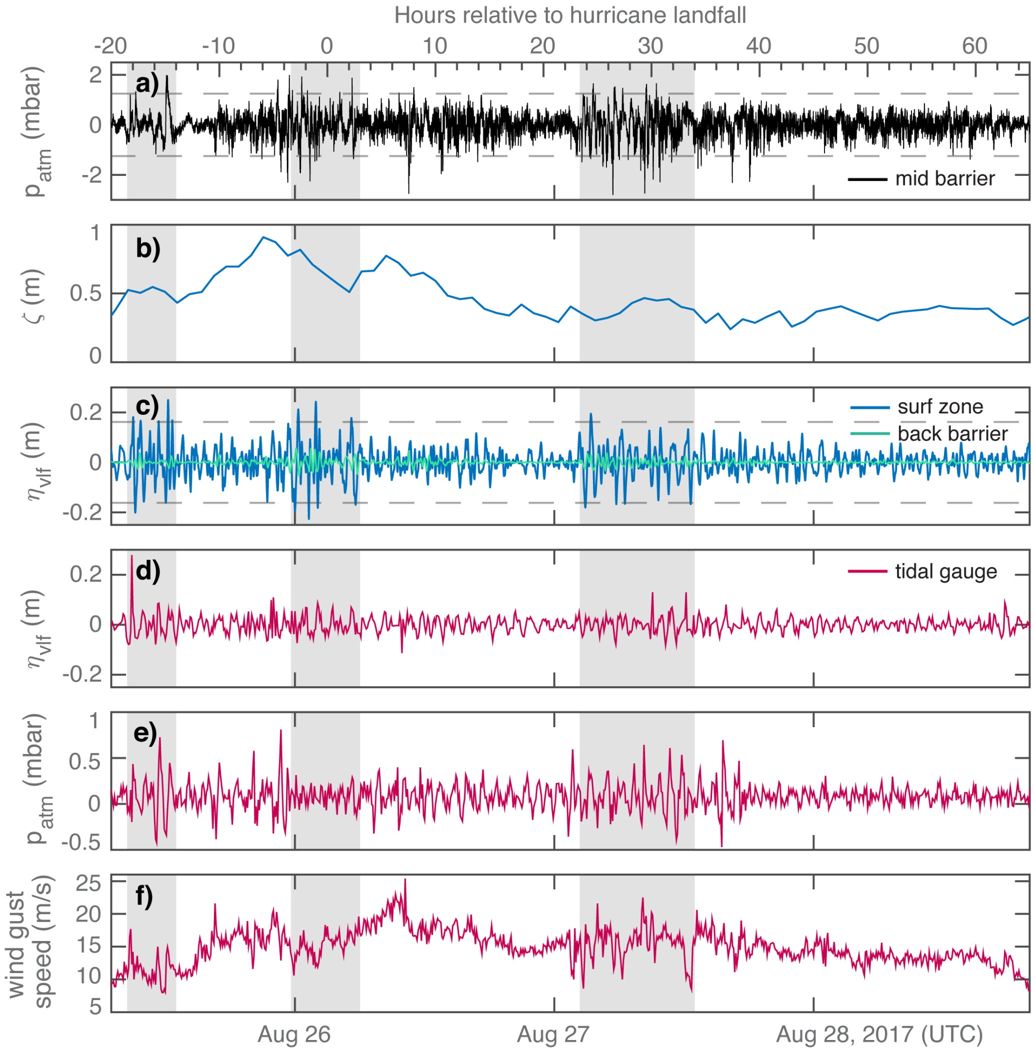

Figure 2. a) Time series of high-frequency air pressure p_{atm}, b) storm surge ζ, and c) VLF sea-level anomalies η_{vlf} in the surf zone and back-barrier at the Follets Island field site; d) η_{vlf}, e) p_{atm}, and f) wind gust speed measured at the NOAA Freeport tidal gauge. Note the different plot scales in (a) and (e). The dashed lines in (a) and (c) denote 3-standard deviations (σ) for p_{atm} (Follets Island) and η_{vlf} (surf zone only). Shaded intervals reflect time periods with sequential instances of η_{vlf} (surf zone) above the 3σ threshold.

The three time periods distinguished by surf zone exceedances of $|\eta_{vlf}|$ above the 3σ threshold were characterized by a wide range of local water levels (0.2-0.9 m storm surge ζ – calculated as the surf zone mean water level minus the predicted astronomical tide – Figure 2b). High resolution measurements of atmospheric (barometric) pressure recorded by a subaerial mounted pressure transducer in the mid-barrier environment at the Follets Island field site (30 sec sampling frequency) revealed that 87% of the 3σ exceedances of $|\eta_{vlf}|$ (surf zone) were preceded within 30 minutes by air pressure disturbances. An air pressure disturbance is here defined as an alternating low-to-high pressure couplet with a peak or trough amplitude that exceeds $|\pm 1.25|$ mbar (dashed lines in Figure 2a). This threshold defines 3 standard deviations of the high-frequency air pressure p_{atm} – that is, the barometric pressure high-pass filtered to remove signals representative of the inverted barometer effect associated with the storm-scale tropical depression (i.e., storm surge $f < 0.1$ mHz). As elaborated upon below, this definition allows for detailed analysis of temporal changes in meteorological forcing throughout the study period. Notably, time series of high-frequency air pressure measured at the Freeport tidal gauge (6-min sampling frequency) did not show pressure anomalies in excess of ± 1.25 mbar (as elaborated upon in Section 4).

On a more regional scale, mosaics of atmospheric radar reflectivity (a measure of precipitation intensity) show that air pressure disturbances measured during all three time periods were concomitant with bands of high reflectivity associated with passage of TCRs. The radar mosaics in Figure 3 depict land-falling TCRs characteristic of each of the three time periods of elevated η_{vlf}. For all three time periods, the radially-propagating TCRs were oriented approximately perpendicular to the coast offshore Follets Island at landfall, however the direction of propagation (from first identification of the TCR in deep water, circles in Figure 3) and structure of the TCRs notably differed for each time period. Early in the storm (-18.5 to -14 hrs), Follets Island is located in the upper right quadrant of the TC, approximately 300 km NE of the TC eyewall (Figure 3a). The land-falling TCRs at the field site during this period were infrequent and radially propagated to the WNW as sub-components of larger outer rainbands that spanned most of the central Texas coast (>200 km in arc-length). As the storm center moved onshore and closer to the field site (eyewall ∼200 km SW), trains of rainbands with very small horizontal scales (<50 km in arc-length, -3 to 3 hrs, Figure 3b) passed frequently over the field site (typically every ∼30 minutes), propagating towards the NW. We classify these very-narrow TCRs as outer rainbands as they are located far outside the inner core region – that is, beyond 3 times the radius of maximum wind as defined by Wang (2009) – which during this time period was very compact (Alford et al., 2019) (∼60 km as estimated from RMS HWind by Brown-Giammanco et al. (2018)). Narrow arc-length TCRs (<75 km) were also observed late in the study period (23.5 to 34 hrs, Figure 3c) when the storm was stalled inland ∼180 km west of the field site. During this time, the land-falling TCRs at Follets Island were oriented slightly more oblique to the coastline and again sub-components of larger outer rainbands (>100 km in arc-length) propagating toward the NE. The forward translation speed of the TCRs across the continental shelf during each of the three time periods was highly variable, ranging from 6 to 29 m/s along the path of a single TCR (as estimated from the reflectivity mosaics). However, the mean forward speeds of the three land-falling TCRs shown in Figure 3 were similar (a,b: 17 m/s and c: 14 m/s).

Surface pressure fluctuations of land-falling TCRs are often characterized by leading pressure troughs followed by pressure ridges, or alternatively low-to-high pressure couplets (e.g. Ligda, 1955; Ushijima, 1958; Hamuro et al., 1969; Yu & Tsai, 2010). The troughs (ridges) of air pressure disturbances measured at Follets Island are delineated with an "L" ("H") in Figure 1a and b. Whilst the identification of pressure couplets is subjective, there is clearly a significant increase in the number of air pressure disturbances for the period proximate to hurricane landfall over early storm conditions, a result of more frequent passage of trains of outer TCRs over the field site. The air pressure disturbances proximate to landfall are also characterized by larger pressure trough amplitudes and

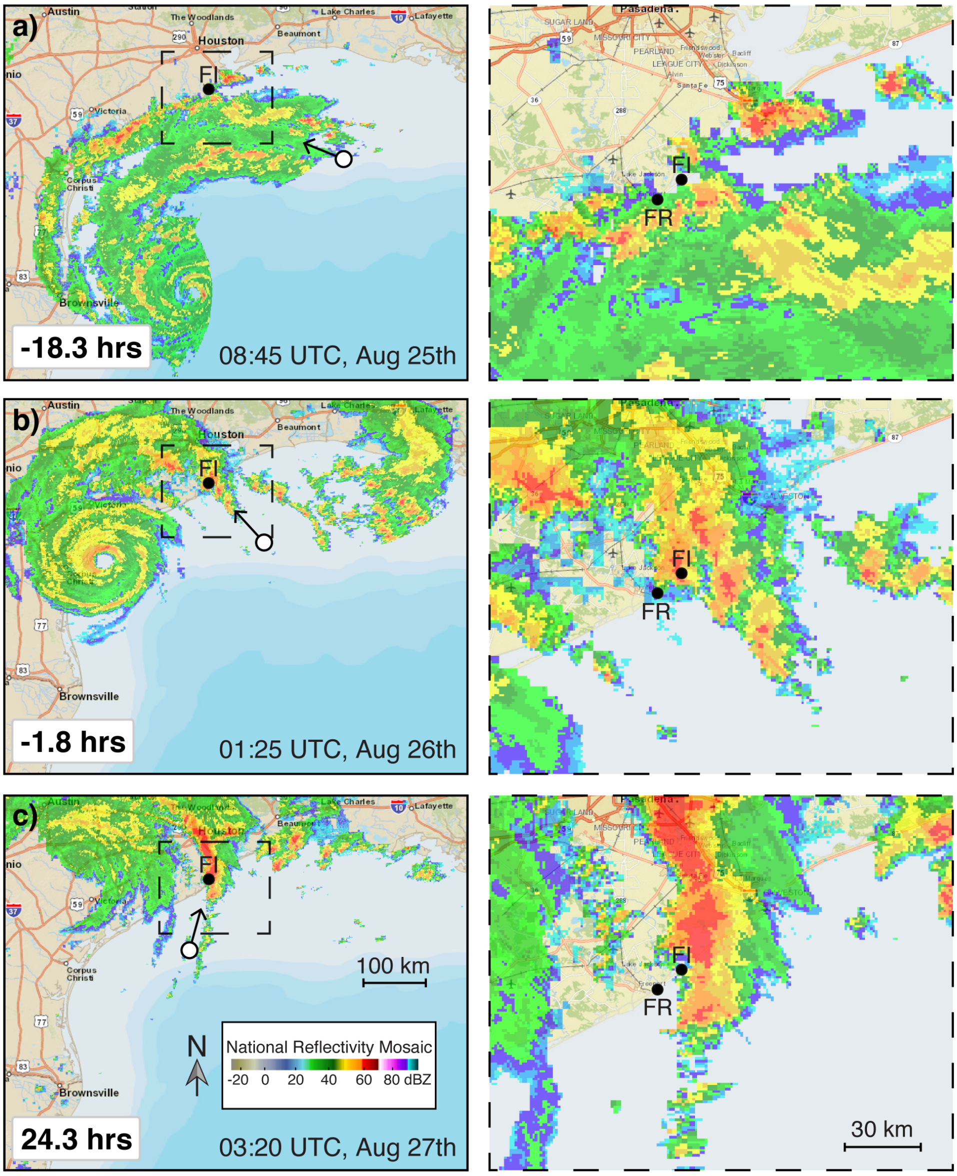

Figure 3. Radar reflectivity mosaics generated by the NOAA National Center of Environmental Information (NCEI-NOAA, 2019) showing bands of high reflectivity associated with land-falling tropical cyclone rainbands (TCRs) preceding instances of elevated η_{vlf} (above the 3σ threshold) during each of the three time periods identified in Figure 2c. Note that the plots on the right depict the TCRs shown in the left at a finer resolution proximate to the Follets Island (FI) field site and the Freeport harbor tidal gauge (FR). The circle and arrow symbols show the direction of propagation of the land-falling TCRs from first identification in deep water.

shorter trough periods than the more infrequent outer TCRs typical of early-storm conditions, despite similar estimated forward speeds at landfall.

The air pressure disturbances highlighted orange in Figure 1g-h were concomitant with passage of the TCRs shown in Figure 3a and b (respectively). Due to the highly-localized nature of the land-falling TCRs during both the period proximate to hurricane landfall (-5 to 0 hrs) and late in the storm (23.5 to 34 hrs), the measured peak and tough amplitudes of the air pressure disturbances may be underestimated. However, for the disturbance highlighted in Figure 1h, radar reflectivity mosaics show that the TCR traversed directly over the Follets Island field site (Figure 3b), which gives high credence to the structure of this pressure couplet. In the following section, we employ a numerical model to explore the generation potential of meteotsunami to a simplified representation of the measured air pressure disturbance highlighted in Figure 1h. This time period is of particular interest since large VLF variability in sea level was only observed in the surf zone and not at nearby tidal gauges. The model is then used in an exploratory framework to better understand potential factors that influence the sea-level response to direct pressure forcing by a very narrow outer TCR.

3 Numerical Modeling

The numerical model utilized in this study is a 2D (depth-integrated) hydrostatic model in spherical coordinates built on the nonlinear shallow water equations, modified to include spatially-dependent air pressure. The governing equations, staggered grid setup, and numerical solution scheme are outlined in Kowalik et al. (2005). The modeling domain encompasses the continental shelf along the eastern GOM and extends landward to include harbors and bays within the greater Freeport and Houston/Galveston region (Figure 4). Bathymetry data was created with a base layer of the NOAA Etopo1 dataset (Amante & Eakins, 2009) (27.5 to 29.9 N, -96.25 to -93.25 W) interpolated to a grid resolution of 6 arcseconds ($\sim$185 m) and referenced to the mean high water. This grid spacing was selected to achieve reasonable simulation time, while satisfying the requirement of having at least 20 grid points to numerically represent the wavelength of the air pressure disturbance. For the Freeport area (28.75 to 29.25 N, -95.5 to -95 W), the baseline grid is superimposed by a 1/9 arcsecond grid (NCEI, 2015) averaged to 6 arcseconds, which allows for high resolution of bathymetric variability within the Freeport Harbor, albeit subaerial structures such as the Freeport jetties are not resolved. The still water level was modified to incorporate the effect of storm surge on water depth for select simulations herein. Bottom friction is based on the Manning model with a Manning coefficient of 0.025 $sm^{(1/3)}$. A coastal wall is set at a water depth of 0.3 m to avoid runup on the $\sim$185-m wide land cells as well as numerical instabilities at zero water depth. Outflow boundary conditions are applied to all the boundaries of the model domain. Model outputs are recorded at the Follets Island surf zone measurement location and the Freeport harbor tidal gauge every 20 seconds. Astronomical tides are not included in the computations.

Due to a lack of spatial information on the characteristics of the air pressure disturbance, we assume a surface pressure function where the amplitude of the crest A_c (0.83 mbar) and trough A_t (2.25 mbar) decay exponentially along the length L of the TCR (23 km)

$$P(x,y) = \begin{cases} A_c * x * exp(-(y)^2 - \left(\frac{x}{L_c}\right)^2),\ x < 0 \\ A_t * x * exp(-(y)^2 - \left(\frac{x}{L_t}\right)^2),\ x > 0 \end{cases} \tag{1}$$

where (x, y) are the longitude and latitude excursions along length L (estimated from radar reflectivity) and L_c and L_t are the wavelength of the pressure crest and trough, respectively. As discussed in more detail below, for the range of forward speeds simulated here, L_c (L_t) spanned 1.8-8.7 km (4.7-22.6 km). Although the path of a TCR is

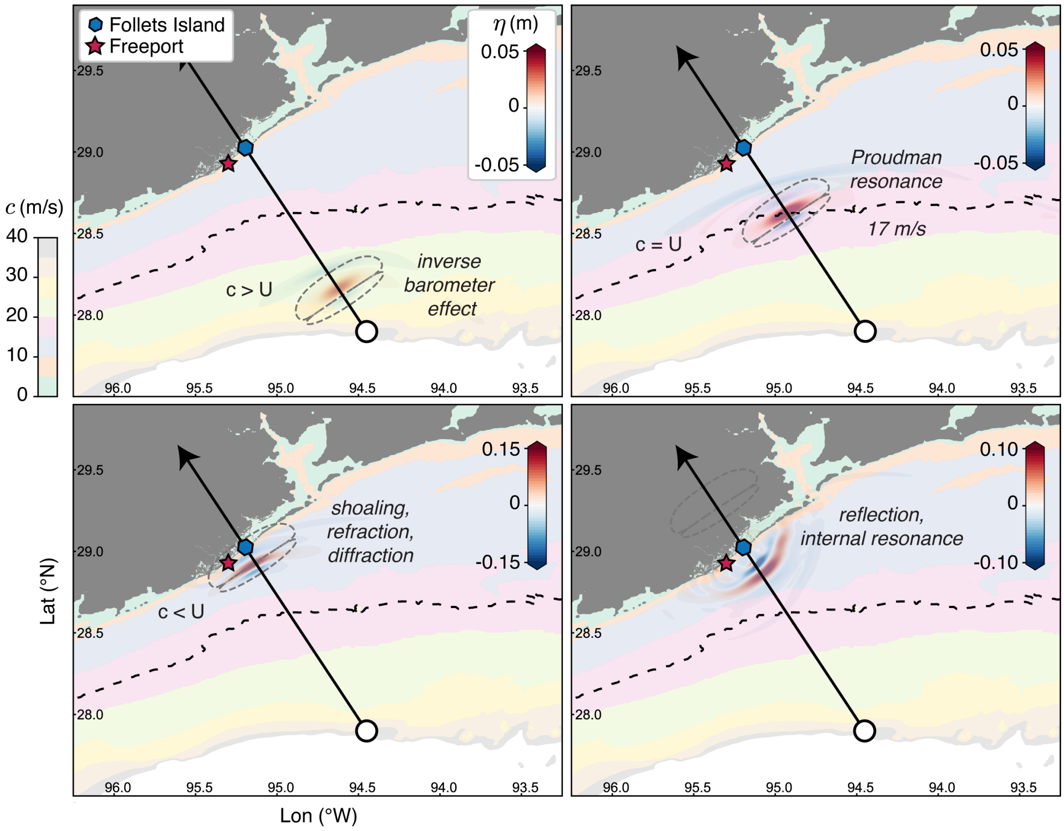

Figure 4. Overview of the model domain and simulated generation mechanism of nearshore meteotsunami by continuous pressure forcing over the continental shelf. The colored contours represent the shallow water wave celerity $c=\sqrt{gh}$ in terms of the water depth h and the blue-red colormap the instantaneous sea-level anomaly η. The bold dashed contour line identifies the location of Proudman resonance – that is, when the speed of the air pressure disturbance U matches c – and maximum energy transfer (here, 17 m/s); the solid black line shows the path along which the disturbance travels (offshore to onshore); and the dashed gray lines indicate the spatial extent of the pressure disturbance.

generally radial, the translation of the pressure disturbance is here simplified to a linear path (single direction) beginning at the edge of the continental shelf and extending inland past the Follets Island field site.

Figure 4 provides an overview of the processes responsible for meteotsunami generation, amplification, and propagation in the numerical simulations, illustrated for the scenario of a 17 m/s TCR forward translation speed U (i.e., the average forward speed of the TCR from radar reflectivity) and 0.71 m of storm surge (as measured in the surf zone during this time period). In deep water, the air pressure disturbance acts on the water surface following the inverse barometer effect. In contrast to storm surge generation (inverse barometer effect acting over large oceanic regions), the subsequent sea-level anomaly is small, on the order of several cm. The celerity of the forced wave (i.e., the Proudman resonance contours) is faster than the speed of the disturbance, which is faintly visible by the blue sea-level trough located ahead of the leading edge of the pressure disturbance. As the air pressure disturbance travels across the shelf, a sea-level perturbation initiated by the inverse barometer effect can grow in height due to Proudman resonance. The forward speed of the TCR determines the region (water depth) where resonant amplification occurs (Proudman resonance) – that is, when the speed of the air disturbance matches the shallow water wave celerity of the region – which in Figure 4 is delineated by a dashed bathymetry contour corresponding to a shallow water wave celerity of 17 m/s (30-m depth). Importantly, the contour of Proudman resonance also demarcates the detachment location at which the resonantly-amplified wave becomes slower than the air pressure disturbance and can thereafter propagate as a free wave. The transformation of the resonantly-amplified wave in the coastal zone through processes such as shoaling, refraction, diffraction, and reflection results in a maximum crest elevation (herein referred to as the "maximum sea-level anomaly") of 0.31 m (peak-to-trough height of 0.47 m) in the surf zone for the 17 m/s scenario. Lastly, while the model can simulate wave amplification by internal resonance processes in coastal bays and harbors, this phenomenon was not clearly evident in any of the numerical simulations described herein.

3.1 Sensitivity to TCR forward speed

Radar reflectivity measurements indicate that the forward translation speed of the TCR varied across the continental shelf between 6 and 29 m/s, which with regard to meteotsunami generation, changes the depth and location of Proudman resonance (Figure 5a). For the bathymetry and coastal morphology offshore Follets Island, TCR forward translation speeds above 17 m/s allow the resonantly-amplified wave to detach from the air pressure disturbance far offshore and thereafter refract towards Freeport. Consequently, Figure 5b shows that for the imposed cross-shelf perpendicular trajectory of the TCR in this study, relatively large meteotsunami (peak-to-trough wave heights >0.25 m) are only observed in the surf zone at Follets Island (Freeport harbor) for a subset of TCR forward speeds, namely 13-24 m/s (17-24 m/s).

The time evolution of simulated and observed pressure and sea level at Follets Island are shown in Figure 5c for the 20- and 24-m/s forward speed scenarios. These scenarios were selected for comparison as they most closely matched 1) the observed lag between passage of the air pressure disturbance (pressure trough) and arrival of the peak sea-level anomaly (the 24 m/s scenario, not shown), and 2) the peak meteotsunami wave height (the 20 m/s scenario, Figure 5b). Note that in order to match the period of the air pressure disturbance at landfall with field observations, the wavelength of the disturbance was varied for each forward speed simulation (6.5-31.3 km, see the changing spatial extent of the dashed lines in Figure 5a). Although the 20 m/s forward speed scenario produces a sea-level anomaly of similar magnitude (observed = 0.24 m, simulated = 0.22 m) and period (observed = 23 min, simulated = 20 min) to the observed VLF anomaly in the surf zone, the lag is shorter than observed (observed = 32 min, simulated = 20 min). Conversely, the simulated peak-to-trough height for the 24 m/s scenario is smaller than observed, despite similar lag times. Lastly, VLF wave heights at the Freeport tidal gauge were <10 cm (Figure 2d) whereas numerically simulated meteotsunami reached 24 and 35 cm in height for the 24- and 20-m/s scenarios, respectively. The source of this mismatch is likely due to model bathymetry, in that the Freeport jetties that shelter the tidal gauge from direct wave impact are not resolved.

While the measured air pressure disturbances can reproduce meteotsunami of similar height and period to the surf zone observations using this simplified model framework, as elaborated upon below, discrepancies between simulated and measured wave characteristics may stem from model uncertainties (bathymetry), model simplification (idealized and temporally-constant representation of the pressure waveform, Williams et al. (2020)), and missing physical processes (wind forcing, Shi et al. (2020)).

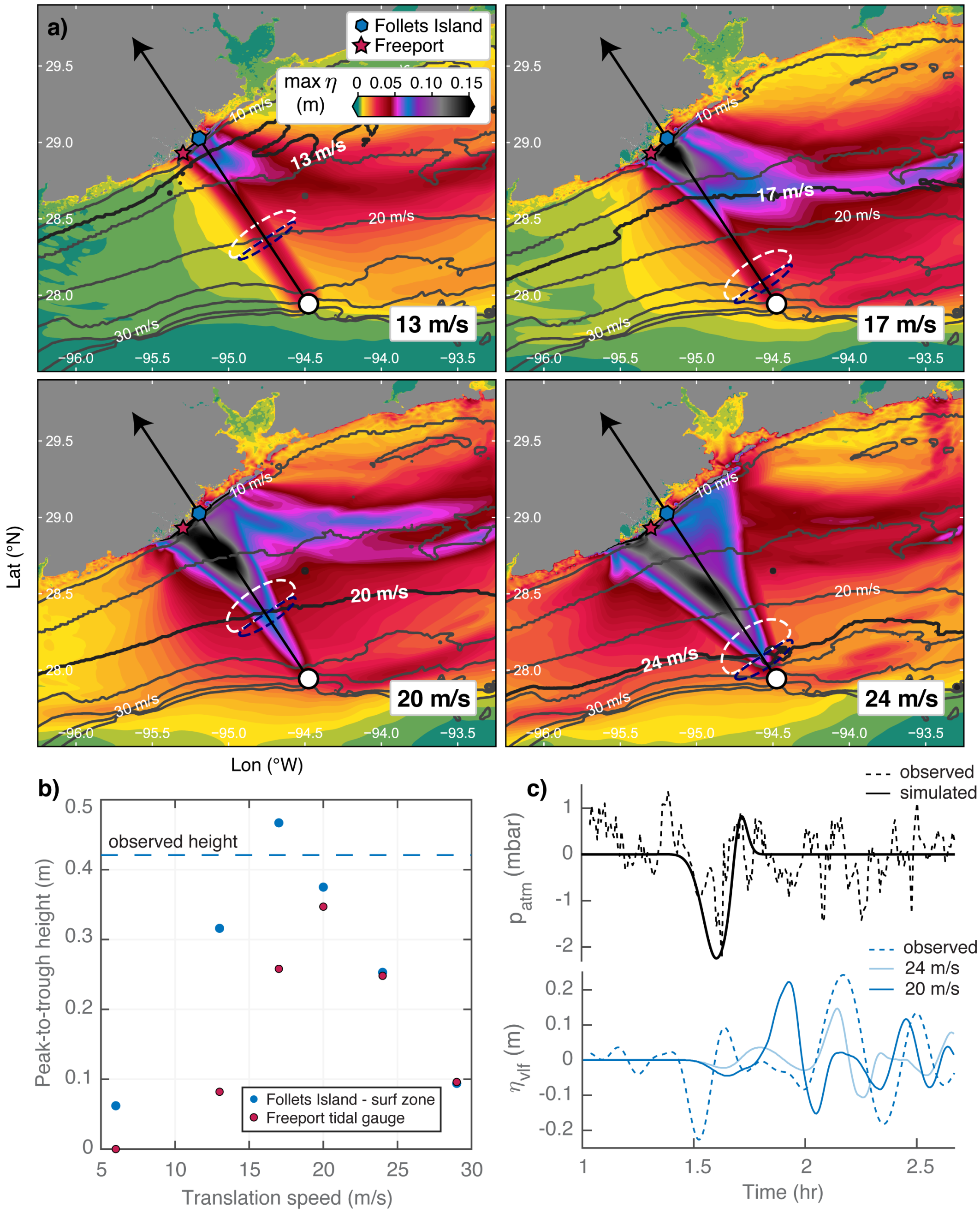

Figure 5. Sensitivity of the simulated a) maximum sea-level anomaly η and b) the maximum peak-to-trough wave height to select TCR forward translation speeds within the range of observations (6-29 m/s). The still water was modified to incorporate the effect of storm surge (0.71 m) on water depth and the dashed line in (b) demarcates the observed peak-to-trough wave height in the surf zone at Follets Island. c) Comparison of the time evolution of the simulated and observed air pressure disturbance (p_{atm}) and sea-level response (20 and 24 m/s only) at Follets Island.

3.2 Sensitivity to storm surge

Using the model setup as an exploratory framework, the sensitivity of meteotsunami generation and propagation to changes in storm surge was examined for variable TCR

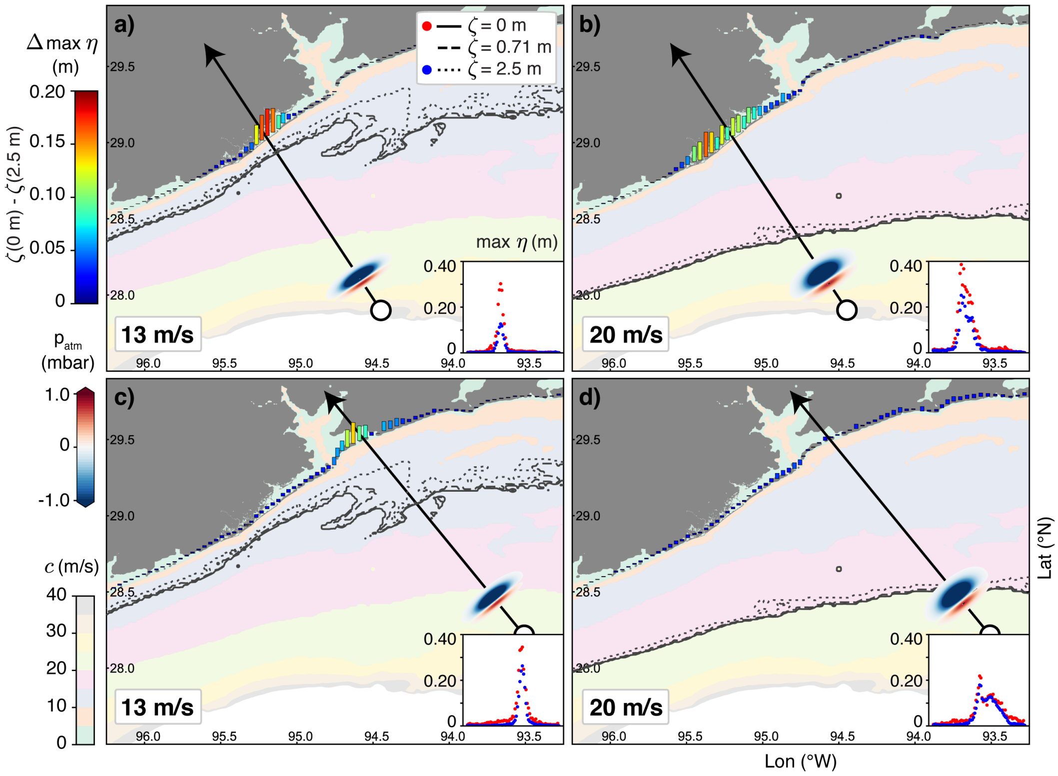

Figure 6. Sensitivity of meteotsunami generation, amplification, and propagation to storm surge ζ for variable TCR forward speeds and landfall locations. Meteotsunami generation varies with surge via the location of Proudman resonance (bold contour lines). Changes in meteotsunami amplification and propagation are depicted by the vertical colored bars which show the difference in the maximum sea-level anomaly η between the case of no surge and the largest simulated surge (2.5 m) along the entire coastline, with the maximum values for each scenario shown in the subplot for direct comparison.

forward translation speeds at both the original Follets Island landfall location (Figure 6a-b) and 80 km to the northeast where the continental shelf is wider (Figure 6c-d). Here we impose a larger surge of ζ=2.5 m (via an increase in still water), which is comparable to the surge at Follets Island during Hurricane Ike in 2008 (2.6 m, Harter & Figlus (2017)).

The vertical colored bars in each pane of Figure 6 show the difference in the maximum sea-level anomaly between the case of zero surge and the 2.5 m surge scenario along the entire coastline for each simulation. In all cases, the effect of storm surge on meteotsunami generation is to increase water depth and thereby move the location of Proudman resonance landward. Hence, the effect of surge on meteotsunami amplification and propagation is complex, and varies both with TCR forward translation speed as well as the offshore bathymetry and coastal morphology. For example, comparing Figure 6a and b, the effect of an increase in surge on meteotsunami hazard (via an increase in the maximum sea-level anomaly at the coast) is larger for a relatively slow moving TCR (13 m/s) than for a relatively fast moving TCR (20 m/s) for TCR landfall at Follets Island. Although the meteotsunami surge response is also sensitive to changes in forward speed farther up the coast (Figures 6c-d), comparison of the two landfall locations shows that the decrease in meteotsunami hazard with an increase in surge is larger at Follets Island due to a slightly steeper sloping continental shelf (i.e., narrower meteotsunami enhancement region). Given the sensitivity of meteotsunami surge response to offshore bathymetry and coastal morphology for our simplified linear TCR trajectory and constant forward speed, it is likely that the effect of surge on meteotsunami hazard is made further complex by more radial TCR translation paths and/or varying speed.

4 Discussion

Many of the VLF sea-level anomalies observed in the nearshore environment along the upper Texas Gulf coast during Hurricane Harvey appear to be initiated by moving-atmospheric disturbances associated with radially-propagating outer TCRs. This hypothesis is supported by numerical modeling of the sea-level response to measured air pressure forcing proximate to hurricane landfall, a time period characterized by frequent passage of very narrow outer TCRs (<50 km in arc-length, Figure 3b) and large air pressure disturbances (1-2 mbar pressure troughs, Figure 1h). The numerical model reproduces meteotsunami similar to the observed VLF sea-level anomalies in the surf zone, albeit the simulated magnitude, period, and spatial extent of meteotsunami hazard (i.e., the maximum sea-level anomaly at the coast) along the open coast is highly dependent on the shelf bathymetry as well as the forward speed and path of translation of the air pressure disturbance (Figure 5). These findings are consistent with other numerical investigations of Proudman resonant wave growth (e.g. Ličer et al., 2017; Shi et al., 2020; Williams et al., 2020). Here we find that the meteotsunami hazard additionally depends on the magnitude of storm surge, which acts to move the location of Proudman resonance landward (Figure 6). For the atmospheric (TCR structure, forward speed, path of translation) and oceanographic (bathymetric configuration) conditions explored in this study, an increase in storm surge results in a decrease in meteotsunami hazard. These numerical results suggest that along this open coastline, meteotsunami hazard is largest for relatively low surge events, like Hurricane Harvey.

It is unknown how increases in model complexity to incorporate additional oceanographic (astronomical tides and currents) and atmospheric factors (radial TCR propagation, variable TCR forward speed, temporal-modifications to the air pressure waveform, wind forcing) will effect meteotsunami hazard, and therefore the relative effect of storm surge for the cases simulated here. Coupled ocean-atmosphere simulations are needed for this purpose, however, to numerically reproduce the high frequency (18 min period) and short wavelength (6.5-31 km, for the range of potential forward speeds) air pressure disturbances measured during Hurricane Harvey, hydrodynamic models need to be forced with higher temporal (<1 min) and spatial (<500 m) meteorological data than used in previous studies (e.g., the 3 km grid spacing and 5 min temporal resolution of the Weather Research and Forecast (WRF) model used by Shi et al. (2020)).

In this study, we focused on the generation potential of meteotsunami by narrow trains of outer TCRs. Shi et al. (2020) showed that meteotsunami can also be triggered by wind and pressure forcing accompanying outer TCRs that are squall-line like in structure. Hence, it is likely that many of the VLF sea-level anomalies identified in the surf zone that were coincident with passage of TCRs that are squall-line like in structure far before (-18.5 to -14 hrs, Figure 3a) and after storm landfall (23.5 to 34 hrs, Figure 3c) are meteotsunami. These observations suggest that, for Hurricane Harvey, meteotsunami hazard spanned several days before and after the peak storm surge (Figure 2) along open coast located to the right of the TC track.

Figure 1 demonstrates that not all atmospheric disturbances were followed by large sea-level anomalies in the surf zone at Follets Island, and notably, only a single sea-level anomaly of comparable magnitude to surf zone observations was measured at regional tidal gauges (0.35 m in peak-to-trough height, Figure 1b). Evaluation of radar reflectivity and meteorological data at the Freeport tidal gauge during this time shows that a squall-line like TCR traversed directly (and nearly perpendicular) over the harbor and it was accompanied by a sharp increase in wind gusts (17 m/s, Figure 2f). Given the orientation of the harbor jetties, it is likely that meteotsunami propagation into this sheltered harbor would require normal incidence, a hypothesis that should be explored further through numerical modeling. Regardless, it is clear from the surf zone observations presented here that during TCs, meteotsunami are more ubiquitous along the open coast than tidal gauge records suggest. This finding likely also stems from the inherent narrow structure of some outer TCR rainbands, which as demonstrated numerically (Figure 5a), trigger meteotsunami with highly-localized propagation and spatial extent (10s of kms). Therefore, efforts to produce flood-risk forecasts that incorporate meteotsunami generation potential by TCRs will require accurate forecasts of individual TCRs during storms, which remains challenging. As the pressure couplets accompanying TCRs are significantly influenced by convective precipitation (Yu & Tsai, 2010; Yu et al., 2018), climate induced changes to TCR convection due to a warming climate may magnify the associated pressure anomalies, and thereby meteotsunami generation via Proudman resonance.

Although meteotsunami were typically small in height in the surf zone during Hurricane Harvey (<42 cm), meteotsunami contributions to the total water level variance in the nearshore were large, reaching a maximum of 23% in the surf zone and 78% in the back-barrier bay at Follets Island. In some cases, meteotsunami wave heights were comparable to the increase in total water level by storm surge (e.g., ∼30-40 cm from -18.5 to -15 hrs and +25 to +35 hrs, Figure 2b). VLF sea-level anomalies were also observed during storm-driven overwash at Matagorda Peninsula, a barrier peninsula located ∼85 km southwest of Follets Island and closer to storm landfall. Anarde et al., (*in review*) hypothesize that these VLF anomalies are likewise meteotsunami triggered by TCRs, and using field data show that the slow variation of total water depth associated with this phenomenon slightly modulate infragravity wave heights during overwash. Although meteotsunami clearly modify storm processes in very shallow water, it is unknown whether meteotsunami are important contributors to sediment suspension and flux. A higher density of field measurements is needed to characterize meteotsunami transformation in the nearshore and the relative contribution of this phenomena to morphological change (i.e., beach and dune erosion) during hurricane impact.

5 Conclusions

Measurements of hydrodynamic and meteorological forcing in the nearshore environment during Hurricane Harvey provide new insights into processes that contribute to meteotsunami hazard along open coasts during TCs. Co-located measurements of sea level and air pressure along the upper Texas coast show that sea-level anomalies in the meteotsunami frequency band (∼8 to 45 min periods) occur with large changes in air pressure accompanying passage of TCRs. It is demonstrated using numerical modeling that drops in air pressure $O(2\text{ mbar})$ concomitant with trains of very narrow outer TCRs (<50 km in arc-length) can trigger meteotsunami similar in period $O(20\text{ min})$ and height $O(0.4\text{ m})$ to surf zone sea-level anomalies. Hence, we find that pressure forcing (air disturbances with periods typically <30 min) accompanying trains of outer TCRs can result in large resonant amplification of sea-level anomalies. This finding is in direct contrast with idealized numerical modeling studies which have shown that the sea-level response to pressure forcing (air disturbances with 1-2 hr periods) accompanying passage of both outer and inner TCRs follows the inverse barometer effect. Our numerical simulations show that the region of Proudman resonance, and thereafter meteotsunami propagation, is highly sensitive to both oceanographic and atmospheric conditions, including TCR forward speed, TCR path of translation, bathymetric configuration, coastal morphology, and storm surge. For this open coast and the very narrow trains of outer TCRs explored here, meteotsunami hazard via Proudman resonance is largest for fast moving

TCRs (13-24 m/s) and low-levels of surge (<1 m). Lastly, comparison of field observations in the surf zone and at neighboring tidal gauges show that meteotsunami are more ubiquitous along the open coast during TCs than tidal gauge records suggest due to the inherent structure and highly-localized propagation of TCRs which likely limits meteotsunami propagation into tidal inlets, harbors, and coastal bays.

Acknowledgments

We thank all members of the COASTRR team for their help with deployment and recovery of field instrumentation in harsh conditions. Funding was provided by the National Science Foundation (NSF) under grant No. OCE-1760713, an Institutional Grant (NA14OAR4170102) to the Texas Sea Grant College Program from the National Sea Grant Office, National Oceanic and Atmospheric Administration. Dr. Figlus received additional support under NSF grant No. OISE-1545837. All views, opinions, findings, conclusions, and recommendations expressed in this material are those of the authors and do no necessarily reflect the opinions of the funding agencies. Further support was provided by Texas A&M University at Galveston and the SSPEED Center at Rice University. Dr. Anarde was additionally supported by the Link Ocean Engineering and Instrumentation PhD Fellowship Program during this project. The data can be obtained via the DesignSafe-CI Data Depot: https://doi.org/10.17603/ds2-m0bc-n829.

References

Alford, A. A., Biggerstaff, M. I., Carrie, G. D., Schroeder, J. L., Hirth, B. D., & Waugh, S. M. (2019). Near-surface maximum winds during the landfall of Hurricane Harvey. *Geophysical Research Letters*, *46*(2), 973–982.

Amante, C., & Eakins, B. (2009). ETOPO1 1 Arc-Minute Global Relief Model: Procedures, Data Sources and Analysis. *NOAA Technical Memorandum NESDIS NGDC-24. National Geophysical Data Center, NOAA.* ([accessed 01-March-2019]) doi: 10.7289/V5C8276M

Blake, E., & Zelinsky, D. (2018). *Hurricane Harvey, National Oceanic and Atmospheric Administration, National Hurricane Center Tropical Cyclone Report* (Tech. Rep.). Retrieved from `https://www.nhc.noaa.gov/data/tcr/AL092017_Harvey.pdf`

Brown-Giammanco, T. M., Giammanco, I., & Pogorzelski, H. (2018). *Hurricane Harvey Wind Damage Investigation* (Tech. Rep.). Insurance Institute for Business & Home Safety.

Churchill, D. D., Houston, S. H., & Bond, N. A. (1995). The Daytona Beach wave of 3–4 July 1992: a shallow-water gravity wave forced by a propagating squall line. *Bulletin of the American Meteorological Society*, *76*(1), 21–32.

Dusek, G., DiVeglio, C., Licate, L., Heilman, L., Kirk, K., Paternostro, C., & Miller, A. (2019). A meteotsunami climatology along the us east coast. *Bulletin of the American Meteorological Society*, *100*(7), 1329–1345.

Haller, M. C., Putrevu, U., Oltman-Shay, J., & Dalrymple, R. A. (1999). Wave group forcing of low frequency surf zone motion. *Coastal Engineering Journal*, *41*(2), 121–136.

Hamuro, M., Kawata, Y., Matsuda, S., Matusno, T., Nakamura, N., Pak, T., ... Yanai, M. (1969). Precipitation bands of Typhoon Vera in 1959 (part I). *Journal of the Meteorological Society of Japan. Ser. II*, *47*(4), 298–309.

Harter, C., & Figlus, J. (2017). Numerical modeling of the morphodynamic response of a low-lying barrier island beach and foredune system inundated during Hurricane Ike using XBeach and CSHORE. *Coastal Engineering*, *120*, 64–74.

Kowalik, Z., Knight, W., Logan, T., & Whitmore, P. (2005). Numerical modeling of the global tsunami: Indonesian tsunami of 26 december 2004. *Science of Tsunami Hazards*, *23*(1), 40–56.

Ličer, M., Mourre, B., Troupin, C., Krietemeyer, A., Jansá, A., & Tintoré, J. (2017). Numerical study of Balearic meteotsunami generation and propagation under synthetic gravity wave forcing. *Ocean Modelling*, *111*, 38–45.

Ligda, M. G. (1955). Hurricane squall lines. *Bulletin of the American Meteorological Society*, *36*(7), 340–342.

Linares, Á., Wu, C. H., Bechle, A. J., Anderson, E. J., & Kristovich, D. A. (2019). Unexpected rip currents induced by a meteotsunami. *Scientific Reports*, *9*(1), 1–9.

Mecking, J., Fogarty, C., Greatbatch, R., Sheng, J., & Mercer, D. (2009). Using atmospheric model output to simulate the meteorological tsunami response to Tropical Storm Helene (2000). *Journal of Geophysical Research: Oceans*, *114*(C10).

Mercer, D., Sheng, J., Greatbatch, R. J., & Bobanović, J. (2002). Barotropic waves generated by storms moving rapidly over shallow water. *Journal of Geophysical Research: Oceans*, *107*(C10), 16–1.

Monserrat, S., Rabinovich, A., et al. (2006). Meteotsunamis: atmospherically induced destructive ocean waves in the tsunami frequency band. *Natural Hazards and Earth System Science*, *6*(6), 1035–1051.

NCEI. (2015). *Digital Elevation Models for the U.S. Coast, NESDIS, NOAA, U.S. Department of Commerce, Boulder, CO.* Retrieved from `https://www.ngdc.noaa.gov/thredds/catalog/tiles/tiled_19as/catalog.html` ([Online; accessed 01-April-2019])

NCEI-NOAA. (2019). *Radar Data Map.* Retrieved from `https://gis.ncdc.noaa.gov/maps/ncei/radar` ([Online; accessed 09-April-2019])

NOAA. (2017). *Freeport SPIP, Freeport Harbor, TX - Station ID: 8772471.* Retrieved from `https://tidesandcurrents.noaa.gov/stationhome.html?id=8772471` ([Online; accessed 10-November-2017])

Olabarrieta, M., Valle-Levinson, A., Martinez, C. J., Pattiaratchi, C., & Shi, L. (2017). Meteotsunamis in the northeastern Gulf of Mexico and their possible link to El Niño Southern Oscillation. *Natural Hazards*, *88*(3), 1325–1346.

Oltman-Shay, J., Howd, P., & Birkemeier, W. (1989). Shear instabilities of the mean longshore current: 2. field observations. *Journal of Geophysical Research: Oceans*, *94*(C12), 18031–18042.

Proudman, J. (1929). The Effects on the Sea of Changes in Atmospheric Pressure. *Geophysical Journal International*, *2*, 197–209.

Rabinovich, A. B. (2019). Twenty-seven years of progress in the science of meteorological tsunamis following the 1992 Daytona Beach event. *Pure and Applied Geophysics*, 1–38.

Shi, L., Olabarrieta, M., Nolan, D. S., & Warner, J. C. (2020). Tropical cyclone rainbands can trigger meteotsunamis. *Nature Communications*, *11*(1), 1–14.

Ushijima, T. (1958). Outer rain bands of typhoons. *Journal of the Meteorological Society of Japan. Ser. II*, *36*(1), 1–10.

Wang, Y. (2009). How do outer spiral rainbands affect tropical cyclone structure and intensity? *Journal of the Atmospheric Sciences*, *66*(5), 1250–1273.

Williams, D. A., Horsburgh, K. J., Schultz, D. M., & Hughes, C. W. (2020). Proudman resonance with tides, bathymetry and variable atmospheric forcings. *Natural Hazards*, 1–26.

Yu, C.-K., Lin, C.-Y., Cheng, L.-W., Luo, J.-S., Wu, C.-C., & Chen, Y. (2018). The degree of prevalence of similarity between outer tropical cyclone rainbands and squall lines. *Scientific Reports*, *8*(1), 8247.

Yu, C.-K., & Tsai, C.-L. (2010). Surface pressure features of landfalling typhoon rainbands and their possible causes. *Journal of the Atmospheric Sciences*, *67*(9), 2893–2911.